

# Monitoring FET flow control and wall adsorption of charged fluorescent dye molecules in nanochannels integrated into a multiple internal reflection infrared waveguide

Youn-Jin Oh,<sup>a</sup> Thomas C. Gamble,<sup>a</sup> Darin Leonhardt,<sup>a</sup> Chan-Hwa Chung,<sup>b</sup> Steven R. J. Brueck,<sup>c</sup> Cornelius F. Ivory,<sup>d</sup> Gabriel P. Lopez,<sup>a</sup> Dimiter N. Petsev<sup>a</sup> and Sang M. Han<sup>\*a</sup>

Received 31st July 2007, Accepted 2nd November 2007

First published as an Advance Article on the web 22nd November 2007

DOI: 10.1039/b711682a

Using Si as the substrate, we have fabricated multiple internal reflection infrared waveguides embedded with a parallel array of nanofluidic channels. The channel width is maintained substantially below the mid-infrared wavelength to minimize infrared scattering from the channel structure and to ensure total internal reflection at the channel bottom. A Pyrex slide is anodically bonded to the top of the waveguide to seal the nanochannels, while simultaneously enabling optical access in the visible range from the top. The Si channel bottom and sidewalls are thermally oxidized to provide an electrically insulating barrier, and the Si substrate surrounding the insulating SiO<sub>2</sub> layer is selectively doped to function as a gate. For fluidic field effect transistor (FET) control, a DC potential is applied to the gate to manipulate the surface charge on SiO<sub>2</sub> channel bottom and sidewalls and therefore their  $\zeta$ -potential. Depending on the polarity and magnitude, the gate potential can accelerate, decelerate, or reverse the flow. Here, we demonstrate that this nanofluidic infrared waveguide can be used to monitor the FET flow control of charged, fluorescent dye molecules during electroosmosis by multiple internal reflection Fourier transform infrared spectroscopy. Laser scanning confocal fluorescence microscopy is simultaneously used to provide a comparison and verification of the IR analysis. Using the infrared technique, we probe the vibrational modes of dye molecules, as well as those of the solvent. The observed infrared absorbance accounts for the amount of dye molecules advancing or retracting in the nanochannels, as well as adsorbing to and desorbing from the channel bottom and sidewalls.

## Introduction

Lab-on-a-chip (LOC) devices have been increasingly used in the last decade for bioseparation, detection, and chemical synthesis.<sup>1–7</sup> These devices have received growing attention because of their speed, efficiency, reduced sample consumption, and detection multiplexing. Many of these advantages led to commercial miniaturized total analysis systems.<sup>1–3</sup> Following the first demonstration of such devices for amino acid<sup>4</sup> and deoxyribonucleic acid (DNA) analysis,<sup>5–7</sup> for instance, microfluidic devices have emerged as a separation platform. More recently, however, nanofluidic devices have been explored to achieve shorter separation time, greater efficiency, and lower sample diffusion than those observed in microscale systems.<sup>8–10</sup> In particular, nanofluidic systems can provide enhanced electroosmotic flow control, compared to microfluidic systems,<sup>11</sup> when the surface charge on

channel walls is manipulated in the presence of significant double layer overlap.<sup>12–14</sup>

This control scheme, where a third potential is applied to a “gate” electrode surrounding the channel walls, is very much analogous to that of the field effect transistors (FETs) used in complementary metal oxide silicon (CMOS) technology. The fluidic devices that use this control scheme are hence termed fluidic FETs.<sup>11,14–16</sup> Since the typical size of biomolecules, the Debye screen length of electrolyte solutions containing the biomolecules, and the size of nanochannels, can be at nearly the same length scale, we expect the nanofluidic FETs to provide enhanced manipulation of biomolecular flow, leading to pronounced separation of biomolecules, while multiple nanochannels ( $>10^4$ ) in an array may simultaneously serve as an integrated detector with increased sensitivity.

Various transport and electrokinetic phenomena in nanofluidic channels, such as electrophoresis, electrostatic control, ion transport, and size and shape effects, have been intensely studied.<sup>17–21</sup> Complementing these studies, herein we demonstrate an *in situ* analytical approach to monitor the average flow speed and localization of molecules in nanochannels during separation. Our approach relies on an experimental platform where nanofluidic channels are integrated into an infrared waveguide. This platform enables multiple internal reflection Fourier transform infrared spectroscopy (MIR-FTIRS) to probe the signature vibrational peaks of molecules

<sup>a</sup>Department of Chemical and Nuclear Engineering, University of New Mexico, Albuquerque, New Mexico, 87131, USA.  
E-mail: meister@unm.edu; Fax: +1 (505) 277 5443;  
Tel: +1 (505) 277 3118

<sup>b</sup>Department of Chemical Engineering, Sungkyunkwan University, Suwon, 440-746, Korea

<sup>c</sup>Center for High Technology Materials, University of New Mexico, Albuquerque, NM, 87106, USA

<sup>d</sup>Department of Chemical Engineering, Washington State University, Pullman, WA, 99164, USA

flowing through the nanochannels. The multi-purpose nanofluidic device is made by conventional Si fabrication technology. The device architecture incorporates a heavily doped Si gate that surrounds the channels to control the surface charge of SiO<sub>2</sub> channel bottom and sidewalls. In this study, we were successfully able to control and monitor the flow of electrolyte solutions containing fluorescent dye molecules by modulating the surface charge and to analyze the interaction between the dye molecules and the internal SiO<sub>2</sub> channel surface, using MIR-FTIRS. The details of our device architecture will be described below.

## Apparatus

To monitor FET flow control and molecular adsorption/desorption in nanochannels, we have fabricated integrated nanofluidic IR waveguides. Two main configurations are used with and without a heavily doped gate that surrounds the nanochannels. The purpose is to compare the effectiveness of flow control, depending on the gate contact resistance. For brevity, we describe our fabrication steps based on the heavily doped gate configuration in Fig. 1. Double-side-polished Si(100) wafers are used as substrates to prevent the scattering and loss of IR beam intensity during multiple internal reflection in our MIR-FTIRS analysis system. Each wafer is diced into rectangular pieces, whose length, width, and thickness are 50, 10, and 0.7 mm, respectively. The rectangular samples are first immersed in Piranha solution to remove the organics and other contaminants on the surface. Piranha solution is prepared by mixing H<sub>2</sub>SO<sub>4</sub> (2 M) with H<sub>2</sub>O<sub>2</sub> (30 wt%) in 4 : 1 volumetric ratio. Piranha is a strong oxidant that forms a thin layer of chemical SiO<sub>2</sub> on Si.<sup>22</sup> The chemical oxide is subsequently removed in dilute HF (Fig. 1(a)), for which 48 wt% HF is mixed with H<sub>2</sub>O in 1 : 10 volumetric ratio. To make the boron doped gate, we first grow a 100 nm thick thermal SiO<sub>2</sub> layer on Si surface. The thermal SiO<sub>2</sub> is represented by a blue middle layer in Fig. 1(b). A 3 mm wide section at the center of the wafer is then etched to expose the underlying Si and allow

boron diffusion, while the remaining SiO<sub>2</sub> layer serves as a mask. A boron dopant, ACCUSPIN<sup>®</sup> B150 spin-on dopant (SOD, Honeywell), represented by a green layer in Fig. 1(b), is spin-coated on the entire top surface. The dopant diffusion is carried out for 60 min at 1050 °C in an O<sub>2</sub>-N<sub>2</sub> environment, which results in the formation of a diffusion layer with a depth of 1–1.2 μm and a dopant level on the order of 10<sup>20</sup> cm<sup>-3</sup>. After the thermal diffusion, the SOD and thermal SiO<sub>2</sub> layer are stripped using a buffered HF solution (Fig. 1(c)). For the ensuing lithographical step, the substrate is coated with an anti-reflective coating (ARC) and a layer of photoresist (PR). These films are represented in brown and blue in Fig. 1(d), respectively. Note that Fig. 1(d)–(i) show dissected mid-section of the fluidic FET device to reveal the nanochannels with clarity. The PR/ARC stack is then exposed to UV laser to create the nanochannel patterns, using interferometric lithography (IL).<sup>23–27</sup> The width of each channel after PR development is approximately 175 nm, and the parallel channels are at 350 nm pitch.

After the IL step, the PR is developed to form a nanochannel mask, exposing the underlying ARC at the channel bottom. A layer of chrome, represented by purple in Fig. 1(f), is then deposited on the developed PR nanochannels. The Cr-PR stacks are subsequently removed by lift-off in acetone, leaving Cr-ARC-covered nanochannel patterns (Fig. 1(g)). These patterns serve as a hard mask that yields a negative image of the previously developed PR patterns. A CHF<sub>3</sub>-O<sub>2</sub> plasma is used to etch high-aspect-ratio nanochannels in the Si substrate (Fig. 1(h)), and an O<sub>2</sub> plasma is used to remove the remaining Cr and ARC (Fig. 1(i)). After creating the Si nanochannels, a thermal SiO<sub>2</sub> layer is grown (1) to insert an electrically insulating layer between the Si channel walls and the fluid and (2) to narrow the channel width to a desired level ( $\leq 100$  nm). Fig. 2(a) and (b) show cross-sectional scanning electron microscope (SEM) images of the nanochannels after the plasma etching step and after the thermal oxidation step. For MIR-FTIRS, the longitudinal ends of the substrate are beveled at 45° and polished (Fig. 1(i)). The oxidized Si nanochannels are finally sealed with a Pyrex slip cover by anodic bonding<sup>19</sup> at 380 °C; 1 kV is applied between the substrate and the Pyrex cover. The Pyrex cover had two 2 mm diameter through holes aligned with opposite ends of the nanochannels. Plastic wells (Nanoports, Upchurch Scientific) are attached to the through holes to facilitate the injection of electrolyte solution containing fluorescent dye molecules (Fig. 3). Fig. 2(c) shows an SEM image of the Pyrex-sealed nanochannel array. Note that since doped Si surrounds only channel bottom and sidewalls, the gate bias controls surface charge only on channel bottom and sidewalls, but not on the channel top Pyrex surface. The width and depth of each channel are approximately 100 and 400–500 nm, respectively. Therefore, a 3 mm *w* × 16 mm *l* nanochannel section contains well over 8000 nanochannels, and if desired, this number can be increased to 10<sup>5</sup> over the 1 cm width of the MIR crystal. We refer to this device as a nanofluidic waveguide, since the device serves simultaneously as a separation matrix and as an analytical tool for MIR-FTIRS.

Fig. 3 conceptually shows how the nanofluidic waveguide is operated. For MIR-FTIRS analysis, a focused IR beam enters

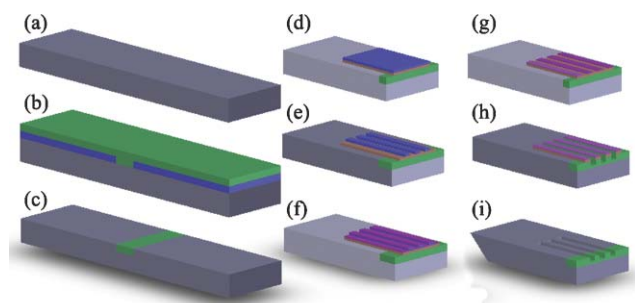


**Fig. 1** Schematic flow diagram of fabrication steps for integrating nanochannels into a MIR waveguide. (a) Cleaned, double-side-polished Si(100) wafer (10 mm × 50 mm × 0.7 mm). (b) Boron SOD-SiO<sub>2</sub> mask for boron diffusion. (c) Highly doped boron gate. (d) PR-ARC mask for interferometric lithography. (e) Nanochannel patterns created by interferometric lithography. (f) Chrome mask to create a negative image. (g) Negative nanochannel patterns after chrome lift-off. (h) Development of nanochannels by plasma etching. (i) Removal of the mask, followed by thermal oxidation and beveling of waveguide edges.

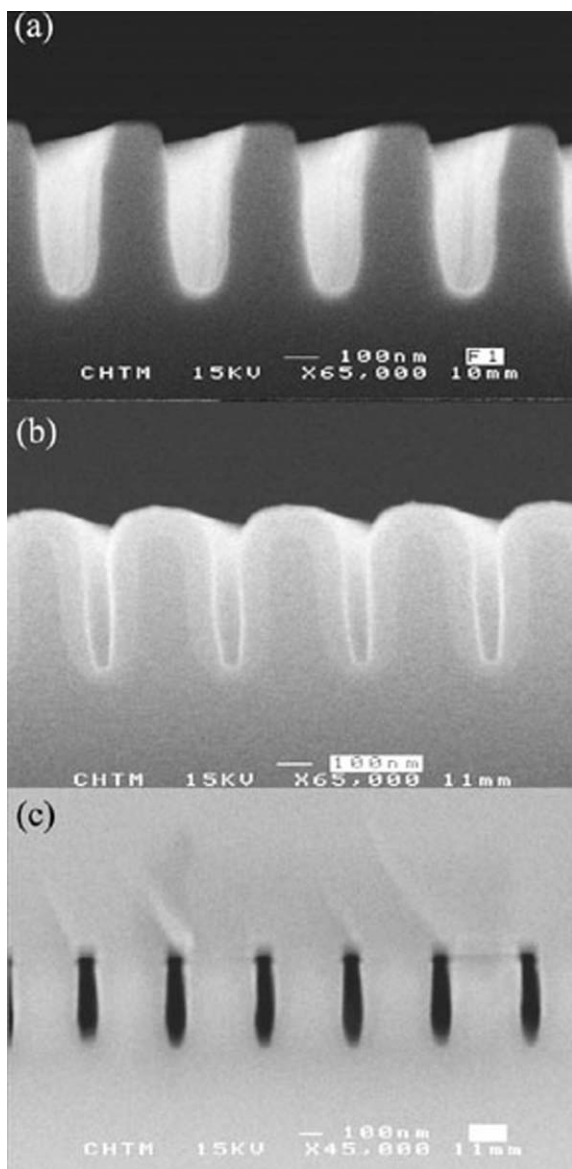


**Fig. 2** Cross-sectional SEM images of nanochannels. (a) Nanochannels after plasma etching. (b) SiO<sub>2</sub>-covered nanochannels after thermal oxidation. The channel width is less than 100 nm, and the depth is 400 to 500 nm. (c) Nanochannels sealed with a Pyrex cover after anodic bonding.

one of the beveled edges of the Si MIR crystal and makes approximately 35 top reflections before the beam exits the opposite end. The IR signal leaving the second beveled edge is collected by a HgCdTe detector. Due to these multiple reflections, the Si MIR crystal is opaque to IR below 1500 cm<sup>-1</sup>.<sup>28,29</sup> Note that the width of the channels is much less than the mid-IR wavelength (2.5 to 15 μm). As the channel width increases to the micrometer level, the IR beam scatters substantially upon each internal reflection, and very little IR passes through the MIR crystal. Since the SiO<sub>2</sub> channel wall and fluid occupy a substantial portion of the channel cross-section, the entire channel area can be approximated as an effective medium that consists of Si, SiO<sub>2</sub>, and water, whose real part of the complex refractive index in the mid-IR region

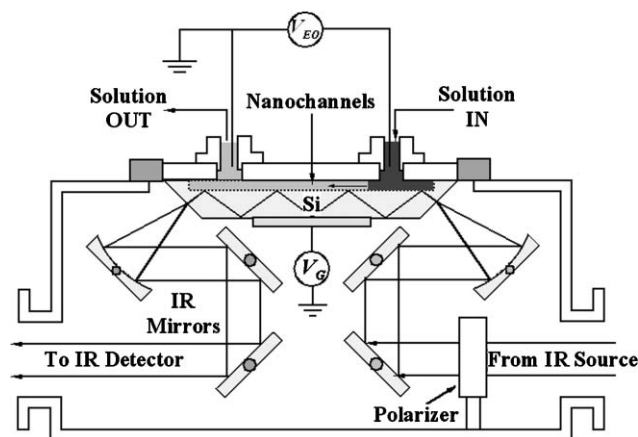


**Fig. 3** Experimental setup to monitor flow control and segregation of dye molecules within nanochannels in response to the gate bias, using MIR-FTIRS. A positive bias ( $V_{EO} = +6$  V) is applied to right hand side well, and the opposite side well is grounded. The gate bias is applied either to a heavily doped or undoped gate.

( $n_{em} \sim 2.28$  based on  $n_{Si} = 3.44$ ,  $n_{SiO_2} = 1.43$ , and  $n_{H_2O} = 1.39$ )<sup>30</sup> is less than that of Si but greater than that of water. The refractive indices of Si, SiO<sub>2</sub>, and H<sub>2</sub>O are average values over the mid-IR range (4000 to 1500 cm<sup>-1</sup>), and the refractive index of the effective medium is calculated by taking a weighed average of the three indices by

$$n_{em} = \frac{w_{Si}}{p} n_{Si} + \frac{w_{SiO_2}}{p} n_{SiO_2} + \frac{w_{H_2O}}{p} n_{H_2O}, \quad (1)$$

where  $w_{Si}$ ,  $w_{SiO_2}$ ,  $w_{H_2O}$ , and  $p$  represent the width of the Si wall, the thickness of SiO<sub>2</sub> layer, the width of open channel occupied by the aqueous solution, and the channel pitch. The critical angle ( $\theta_c$ ) calculated from  $n_{em} \sim 2.28$  and  $n_{Si} = 3.44$  is 41.5°. Thus, we expect the IR beam to undergo multiple total internal reflections between the channel bottom surface and the Si substrate bottom surface, and the evanescent wave at the channel bottom to decay exponentially into the channel fluid. The characteristic depth of penetration ( $d_p$ ) of the evanescent wave is proportional to IR wavelength ( $\lambda$ ) according to

$$d_p = \frac{\lambda/n_{Si}}{2\pi \left( \sin^2 \theta - \left( \frac{n_{em}}{n_{Si}} \right)^2 \right)^{1/2}}, \quad (2)$$

where  $\theta$  represents the angle of incidence at 45°. For the mid-IR range (4000 to 1500 cm<sup>-1</sup>) accessible with Si waveguides,  $d_p$  ranges from 0.47 to 1.25 μm. Therefore, the evanescent wave probes the entire channel depth.

To monitor the electroosmotic (EO) flow in nanochannels with MIR-FTIRS and with laser-scanning confocal fluorescence microscopy (LS-CFM, Zeiss Axioskop with an LSM5 scanning head), the nanochannels are first filled completely with a desired buffer solution by capillary force. The LS-CFM technique is considered a standard optical technique to monitor the flow of fluorescent dye molecules in nanochannels and is used here to provide a baseline comparison with the MIR-FTIRS technique. We note that the depth of focus for

LS-CFM is limited to 1  $\mu\text{m}$ , which disallows depth profiling 400 nm deep channels. Thus, optical images are averaged over the entire channel depth. A platinum wire is then inserted into each well as an electrode. We apply a positive potential ( $V_{\text{EO}} > 0$ ) to one well, while grounding the other (Fig. 3). This potential difference creates a longitudinal electric field ( $\vec{E}$ ) along the channels and induces the EO flow. While the EO flow is in motion, we inject into the positively biased well, fluorescent dye molecules pre-dissolved in the identical buffer solution. The gate potential ( $V_{\text{G}}$ ) is then applied to control the surface charge on the channel walls. We observe the motion of fluorescent dye molecules under EO flow and upon modulating  $V_{\text{G}}$ , using both MIR-FTIRS and LS-CFM for purposes of comparison.

## Experimental

Since the vibrational modes of  $\text{H}_2\text{O}$  (3000–3400  $\text{cm}^{-1}$  and 1640  $\text{cm}^{-1}$ ) in the mid-IR region could significantly overlap with those of fluorescent dye molecules,  $\text{D}_2\text{O}$  is used in all of our experiments instead of  $\text{H}_2\text{O}$ . We also use two kinds of buffer solutions: (1) acetate buffer for low pH and (2) tris-glycine buffer for high pH. The pH of 1 mM acetate buffer ( $\text{p}K_{\text{a}} = 4.76$ ) in  $\text{D}_2\text{O}$  is adjusted to 4 by adding HCl. The tris-glycine buffer contains 0.25 mM tris-(hydroxy)aminomethane hydrochloride and 1.92 mM glycine. Then, the pH is adjusted to 10 by adding NaOH. The ionic strength of these buffer solutions is estimated to be around 1 mM and 0.35 mM, respectively. At this ionic strength, we calculate the magnitude of the Debye screening length,  $1/\kappa$ , to be approximately 10 and 20 nm, where  $\kappa$  is given by

$$\kappa^2 = \frac{e^2}{\epsilon\epsilon_0 k_{\text{B}} T} \sum_i z_i^2 n_i, \quad (3)$$

where  $e$ ,  $\epsilon$ ,  $\epsilon_0$ ,  $k_{\text{B}}$ ,  $T$ ,  $z_i$ , and  $n_i$  represent unit charge, dielectric permittivity, vacuum dielectric constant, Boltzmann's constant, temperature, valence charge, and charge density, respectively.

The pH of the buffer solution determines the sign and magnitude of the surface charge on the channel walls. That is, the inherent  $\zeta$ -potential and the capacitance of the diffuse layer are changed according to the pH of the buffer solution. These changes affect the control of surface charge on the channel walls and the EO flow. For the  $\text{SiO}_2$  channel walls, the isoelectric point is approximately at  $\text{pH} = 3.7$ , where the net charge on the surface is zero.<sup>31</sup> Above the isoelectric point (*i.e.*,  $\text{pH} > 3.7$ ), the surface charge becomes increasingly negative as surface hydroxyl groups ( $\text{SiOH}$ ) become deprotonated. Ghowsi *et al.* and later Schasfoort *et al.* have demonstrated that the  $\zeta$ -potential control, and therefore EO flow control, are most pronounced near the isoelectric point.<sup>11,15,16</sup> Thus, we set the pH of our buffer solutions close to 4 to facilitate the  $\zeta$ -potential control and compare the results with buffer solutions of pH close to 10. The reason for choosing  $\text{pH} = 4$  and  $\sim 10$  for comparison is to observe the effect of positive *vs.* negative charges of fluorescent dye molecules on molecule–wall interactions. Rhodamine B (MW = 479),  $\text{C}_{28}\text{H}_{31}\text{ClN}_2\text{O}_3$ , fluorescent dye molecule is dissolved in the

previously described buffer solutions in our experiments. Rhodamine B is positively charged, neutral, and negatively charged in the pH range below 6.0, 6.0 to 10.8, and above 10.8, respectively.<sup>32,33</sup>

## Results and discussion

FET flow control experiments are conducted with Rhodamine B (MW = 479),  $\text{C}_{28}\text{H}_{31}\text{ClN}_2\text{O}_3$ , dissolved in a pH 4 buffer solution previously described. After filling the nanochannels with only the buffer, we initiate the EO flow by applying +6 V ( $V_{\text{EO}}$ ) to one of the wells, while the opposite well is grounded, and the gate is left floating (Fig. 3). In this case, the gate is heavily doped to minimize the contact resistance. Fig. 4 shows the LS-CFM images of Rhodamine B under FET control. Note that within the field of view, approximately 5000 channels are present, extending horizontally in Fig. 4. Since the channel width is below the diffraction limit, adjacent nanochannels cannot be optically distinguished. The non-uniformity in channel dimensions across the waveguide leads to a non-uniform, irregular moving front in Fig. 4, as the dye molecules traverse farther into the channels. The dimensional uniformity amongst nanochannels will have to improve to achieve a uniform moving front.

In Fig. 4, the dotted lines mark the reference point, and the arrows mark the direction and magnitude of the dye flow. The observed EO flow velocity is  $2 \mu\text{m s}^{-1}$ . When a negative gate bias ( $V_{\text{G}} = -30 \text{ V}$ ) is applied to produce a large negative  $\zeta$ -potential, the flow velocity is increased to  $6 \mu\text{m s}^{-1}$ . In Fig. 4(a)–(b), Rhodamine B moves from right to left at an

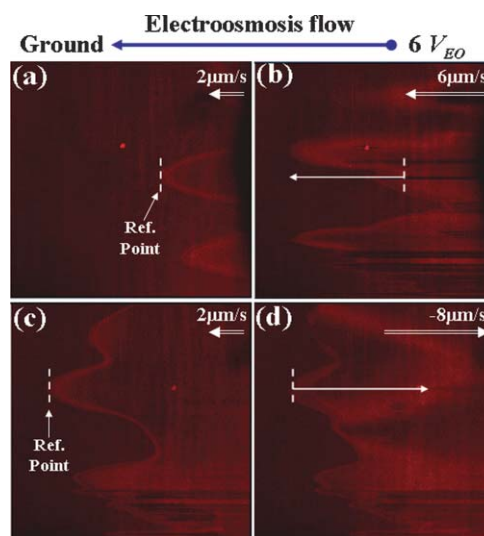


**Fig. 4** LS-CFM images of Rhodamine B in a pH 4 buffer solution under electroosmotic flow, with and without the gate bias. (a)–(b) show the acceleration of electroosmotic flow with negative gate bias. The initial flow rate of Rhodamine B under electroosmotic flow is  $2 \mu\text{m s}^{-1}$  (Fig. 4(a)), and the flow accelerates to  $6 \mu\text{m s}^{-1}$  upon applying a negative gate bias ( $V_{\text{G}} = -30 \text{ V}$ ) (Fig. 4(b)). (c)–(d) show the reversed electroosmotic flow with positive gate bias. Rhodamine B flows in the reverse direction at  $-8 \mu\text{m s}^{-1}$  upon applying a positive gate bias ( $V_{\text{G}} = +30 \text{ V}$ ). The outline of the flow front remains at the same place, indicating strong wall adsorption of positively charged Rhodamine B in pH 4 buffer.

accelerated pace. Conversely, Fig. 4(c)–(d) shows that Rhodamine B rapidly reverses its flow at  $-8 \mu\text{m s}^{-1}$  when  $+30 \text{ V}$  is applied to the gate. The flow response to the change in the gate bias is immediate and repeatable. The observed flow response is also independent of the position of dye molecules with respect to the gate position. That is, the flow response is identical, independent of whether the dye molecules are either side of the gate region.

To determine the impact of gate contact resistance, the above experiment is repeated with the undoped gate configuration. In this case, the flow of Rhodamine B does not accelerate or reverse upon applying a negative or positive gate bias within the range of  $V_G$  from  $-30$  and  $+30 \text{ V}$ . Even with a high positive gate bias ( $V_G = +50$ – $60 \text{ V}$ ), the flow is reversed only to a velocity of  $-2 \mu\text{m s}^{-1}$ . These results show that the flow control is easier with the heavily doped gate. That is, when the Si substrate is not doped, a sufficient voltage drop appears to exist across the metal–silicon (Cr–Si) contact and through the Si substrate that meets the  $\text{SiO}_2$  channel walls. We observe minimal but detectable leakage current density on the order of  $\text{nA cm}^{-2}$  through the gate  $\text{SiO}_2$ , and this entails that the actual potential applied to the channel walls must be below the applied gate bias, due to the potential drop across the Cr–Si contact and through the bulk Si. The magnitude and influence of the leakage current on FET flow control will be discussed in detail in our future publication. Since we observe a threshold gate bias on the order of  $\pm 10 \text{ V}$  that leads to measurable FET flow control with the heavily doped gate, the apparent voltage drop across the Cr–Si contact and through the undoped Si substrate must be sufficient enough to reduce the actual applied voltage below the threshold. In our case, the gate contact is also made on the top side near the edge of the  $1 \text{ cm}$  wide MIR crystal, and the heavily doped gate ensures uniformly applied gate bias around the channel walls, whereas the undoped gate would introduce an asymmetry and a significantly long resistive path around the 8000 channels, leading to a decreasing potential from the first channel closest to the gate contact to the last channel farthest away from the gate contact. We suspect that these reasons contribute to the pronounced FET control with the doped gate.

According to the above argument, the heavily doped gate is also suspected to provide a uniform potential around the array of nanochannels and therefore a uniform  $\zeta$ -potential on  $\text{SiO}_2$  channel walls surrounded by the doped gate region. Although a variation of  $\zeta$ -potential is suspected from the doped gate region to the undoped bulk Si, the local  $\zeta$ -potential control is shown to be sufficient enough to cause the electroosmotic flow to accelerate or decelerate. This local doping avoids having to dope the entire Si substrate. The localized control of  $\zeta$ -potential by the heavily doped isolated gate would also prove effective, if one desires local pH control in the nanochannels. We have experimentally measured, using laser induced fluorescence from SNARF-1 and IR peak shift of fluorescein pH indicator, that the deprotonation of SiOH is sufficient enough to cause a decrease in pH from 7 to 6 when a pH = 7 phosphate-based buffer is introduced into the nanochannels. With the gate biasing, this pH shift can be further enhanced by another pH unit. We will fully discuss this pH shift by heavily doped multiple gates in our future work.

From our results, the flow control with Rhodamine B shows a limitation when the flow is reversed (Fig. 4(d)). We observe that most of Rhodamine B flows in the reverse direction, marked by the solid arrow, while the left-most outline of Rhodamine B, marked with the dotted reference line, remains at the same position. This observation indicates that potentially two layers of Rhodamine B exist in the nanochannels because Rhodamine B is positively charged in the pH range below 6.0, while the surface of the nanochannels is negatively charged. We hypothesize that an inner layer, away from the channel walls, is controllable, while the outer layer near the channel walls is not, due to the electrostatic interaction between positively charged dye molecules and negatively charged channel walls. That is, the dye molecules are likely to adsorb and concentrate near the channel walls.

Our hypothesis is supported by MIR-FTIR analysis during FET flow control. The IR background spectrum is recorded after completely filling the nanochannels and inlet/outlet wells with the buffer solution and injecting Rhodamine B into the positive well. While the dye molecules flow into the nanochannels due to electroosmosis and respond to the gate bias, the sample spectra are taken every 5 min with  $2 \text{ cm}^{-1}$  resolution (Fig. 5). Each spectrum is averaged over 50 scans to achieve a good signal-to-noise ratio, while maintaining a reasonable time resolution. Fig. 6(a) shows representative IR absorbance spectra extracted from Fig. 5, taken during electroosmosis for different gate voltages. We observe the O–D stretching vibration modes of  $\text{D}_2\text{O}$  at  $2800$ – $2200 \text{ cm}^{-1}$  as well as O–D and O–H stretching vibration modes of HDO at  $2600$ – $2500 \text{ cm}^{-1}$  and  $3600$ – $3200 \text{ cm}^{-1}$ , respectively.<sup>34,35</sup> We suspect that proton exchange amongst  $\text{D}_2\text{O}$ , buffer molecules, dye molecules, and SiOH groups in thermal  $\text{SiO}_2$  leads to observed random fluctuations in O–H and O–D stretching vibrational modes.

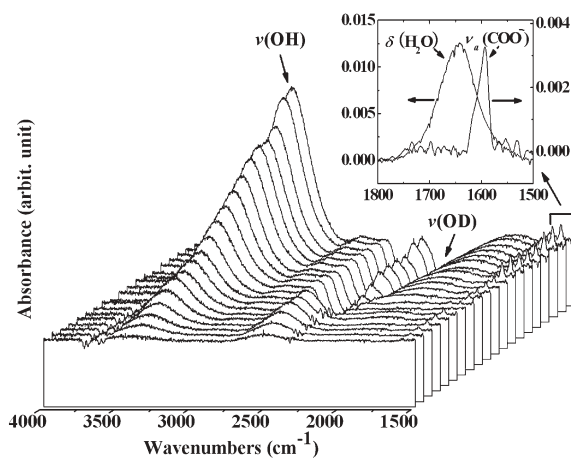


**Fig. 5** A time-series IR absorbance spectra of Rhodamine B in  $\text{D}_2\text{O}$  taken during FET flow control. The background spectrum is taken after filling the nanochannels with a  $\text{D}_2\text{O}$  buffer solution. The sample spectra are taken every 5 min, while Rhodamine B flows into the nanochannels by electroosmosis. The O–D stretching vibrational modes of  $\text{D}_2\text{O}$  at  $2800$ – $2200 \text{ cm}^{-1}$ , as well as O–D and O–H stretching vibrational modes of HDO at  $2600$ – $2500 \text{ cm}^{-1}$  and  $3600$ – $3200 \text{ cm}^{-1}$  are observed. The inset shows that  $\text{COO}^-$  of Rhodamine B at  $1590$ – $1600 \text{ cm}^{-1}$  is distinguishable from  $\text{H}_2\text{O}$  scissoring mode at  $1640 \text{ cm}^{-1}$ .

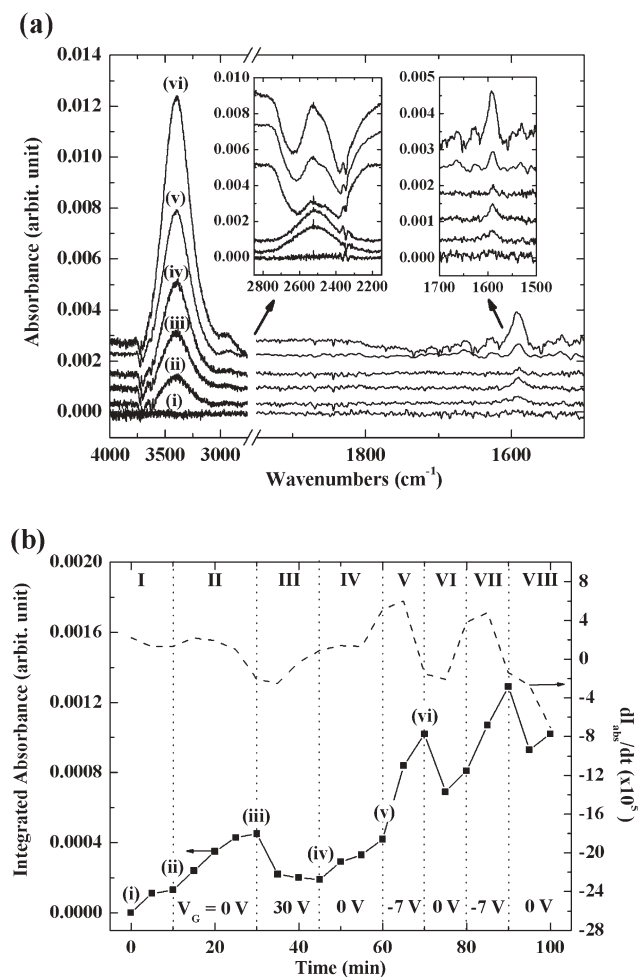


**Fig. 6** MIR-FTIR analysis of flow control, segregation, and adsorption/desorption of Rhodamine B in pH 4 buffer within nanochannels. The dye molecule is positively charged at pH 4. (a) A representative set of IR spectra taken during electroosmotic flow in response to the gate bias. The left-hand-side inset shows random fluctuations of O–D stretching vibrational mode. The right-hand-side inset shows the stretching vibrational mode of COO<sup>−</sup>. (b) Changes in the integrated absorbance of COO<sup>−</sup> peak in response to the electroosmotic flow and to the gate bias.

Typical vibrational peaks of powder-form Rhodamine B are observed at 3068, 2960, 2923, 2849, 1700, 1590, and 1548 cm<sup>−1</sup>.<sup>36</sup> However, the vibrational modes near 3068–2849 cm<sup>−1</sup> overlap with the broad O–H stretching vibrational mode. Thus, we focus on the asymmetric stretching vibrational mode of COO<sup>−</sup> at 1590–1600 cm<sup>−1</sup>, which is the strongest vibrational mode of Rhodamine B (inset of Fig. 5 and second inset of Fig. 6(a)).<sup>37</sup> We also note that the COO<sup>−</sup> stretching mode is clearly distinguishable from the scissoring mode of H<sub>2</sub>O, which is typically shown at 1640 cm<sup>−1</sup> (inset of Fig. 5). Scissoring modes of H<sub>2</sub>O, D<sub>2</sub>O, and HDO are assigned at 1640, 1210, and 1450 cm<sup>−1</sup>, respectively.<sup>38</sup> The increase and/or decrease in the intensity of the COO<sup>−</sup> peak represents: a convolution of an increasing amount of Rhodamine B filling the channels during electroosmosis and upon applying a negative gate bias; increasing concentration of Rhodamine B near the channel bottoms and sidewalls as a electrostatic

response to negative gate bias; decreasing amount of Rhodamine B during reverse flow with a positive gate bias; and decreasing concentration of Rhodamine B near the channel bottoms and sidewalls as an electrostatic response to positive gate bias.

Fig. 6(a) shows a representative sample spectra corresponding to the initial state before Rhodamine B enters the channels and the subsequent spectral changes during electroosmosis with a grounded gate ( $V_G = 0$  V), upon applying a positive gate bias ( $V_G = +30$  V), and upon applying a negative gate bias ( $V_G = -7$  V). The variation in the intensity of the COO<sup>−</sup> peak is then plotted in Fig. 6(b) as a function of time in response to different gate voltages. Spectrum (i) in Fig. 6(a) represents the initial state, while spectrum (ii) is recorded 10 min after injecting the dye molecules into the inlet well but before the electroosmotic flow is induced. In the absence of applied voltages, where only diffusion would take place, the IR intensity of the COO<sup>−</sup> peak slightly increases and levels off due to the diffusion of Rhodamine B into the nanochannels observed by LS-CFM, as well as ensuing wall adsorption. This corresponds to the region for  $t = 0$ –10 min (period I) in Fig. 6(b). We speculate that the positively charged Rhodamine B and negatively charged SiO<sub>2</sub> channel walls also facilitate this initial diffusion and increase in the peak intensity. The length of diffusion observed by LS-CFM is 0.24 mm over 10 min, and we estimate the effective diffusion constant to be  $4 \times 10^{-6}$  cm<sup>2</sup> s<sup>−1</sup>. This is an upper limit for the diffusion of charged molecules due to favorable attractive interactions with the channel wall, and we expect the magnitude of the effective diffusion constant to be more pronounced in the transverse direction than in the longitudinal direction to the channel orientation. However, the characteristic length of diffusion in both directions is an order of magnitude lower than the transport length by EO.

Spectrum (iii) shows an increase in the COO<sup>−</sup> peak intensity upon applying  $V_{EO} = +6$  V with a grounded gate ( $V_G = 0$  V). This increase in intensity is due to Rhodamine B flowing into the nanochannels by electroosmosis. The rate of increase during electroosmosis, representing the average flow speed of Rhodamine B in the nanochannels, is approximately the same as the rate of initial diffusion. The corresponding intensity plot is from 10 to 30 min (period II) in Fig. 6(b). When a positive gate bias ( $V_G = +30$  V) is applied, while  $V_{EO}$  is set at +6 V to maintain the electroosmotic flow, the flow direction is reversed. The intensity immediately decreases for  $t = 30$ –45 min (period III) in Fig. 6(b). This corresponds to spectrum (iv) in Fig. 6(a). The intensity increases again when the gate bias ( $V_G = +30$  V) is turned off under  $V_{EO} = +6$  V (period IV), following the same slope as  $t = 10$  to 30 min (period II) and increases rapidly when a gate bias of  $V_G = -7$  V is applied (see spectra (v–vi) in Fig. 6(a)). This rapid increase is due to the acceleration of the dye molecules, as well as the positively charged dye molecules electrostatically responding to the negative gate bias and accumulating near the channel bottoms and sidewalls.

One can approximate the latter electrostatic contribution by turning off the gate bias and measuring the decrease in IR absorbance (period VI), despite the continuous electroosmotic flow of dye molecules into the channels. We deduce that this

decrease IR absorbance is due to the release of positively charged Rhodamine B molecules at pH = 4, previously accumulated near the negatively charged surface in response to the negative gate bias. However, the transient decrease in IR absorbance eventually ceases, counter-balanced by the continuous electroosmotic flow, and the absorbance starts to increase again towards the end of period VI. The electrostatic contribution to the IR absorbance increase is repeatedly measured (see period VII–VIII in Fig. 6(b)).

To further test our hypothesis regarding the electrostatic response of charged dye molecules in response to the polarity of the gate bias, the above experiment is repeated with Rhodamine B in pH  $\sim 10$  buffer solution, in which Rhodamine B is negatively charged. Fig. 7 shows the changes in the IR absorbance of COO<sup>-</sup> vs. time in the pH 10 buffer solution in response to both  $V_{EO}$  and  $V_G$ . Due to electrostatic repulsion between negatively charged dye molecules and negatively charged channel surface, no diffusion is observed in the absence of applied voltages. Only when a potential drop ( $V_{EO} = +6$  V) is applied, the intensity begins to increase at  $t = 20$  min as Rhodamine B flows into the nanochannels due to electroosmosis. When  $V_G = +30$  V is applied at  $t = 35$  min, the intensity rapidly increases, even though the flow direction of dye molecules is reversed with the positive gate bias, suggesting that a substantial amount of dye molecules accumulate near or adsorb onto the channel bottoms and sidewalls. This increase in IR absorbance is reversed at  $t = 50$  min, when the gate bias is turned off, and the Rhodamine B molecules previously accumulated or adsorbed are partially released. Our observation indicates that the accumulation and adsorption of negatively charged Rhodamine B can substantially contribute to the increase in IR absorbance. For instance, turning off the gate bias does not completely reverse the accumulation/adsorption of dye molecules, as applying a negative gate bias ( $V_G = -7$  V) leads to a further decrease in IR absorbance ( $t = 60$  to 65 min), while the accelerated flow is induced. That is, the dye molecules may irreversibly adsorb onto the channel bottom and sidewalls. This enhanced decrease in IR

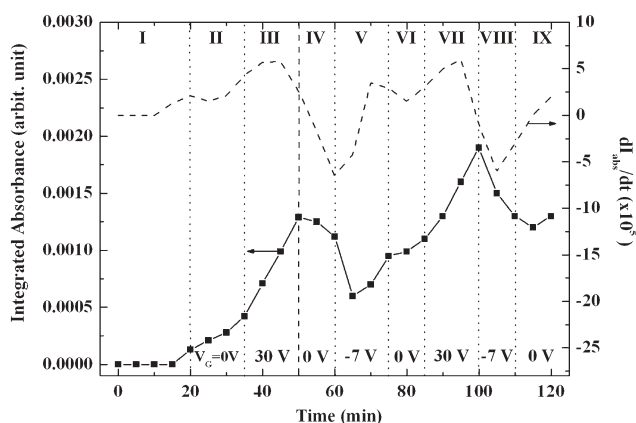


**Fig. 7** MIR-FTIR analysis of flow control, segregation, and adsorption/desorption of Rhodamine B in pH 10 buffer within nanochannels. The dye molecule is negatively charged at pH 10. Changes in the integrated absorbance of COO<sup>-</sup> peak captures acceleration/deceleration of the dye flow, convoluted with wall adsorption/desorption in response to the gate bias.

absorbance with the negative gate bias is eventually counter-balanced by the accelerated electroosmotic flow, and the IR absorbance increases again ( $t = 65$  to 75 min). This cycle of accumulation/adsorption and repulsion/desorption in response to the changes in the surface charge on the channel walls is repeatedly measured by modulating the gate bias with our integrated MIR-FTIR setup.

In order to eliminate or mitigate the irreversible wall adsorption of charged molecules, while taking advantage of FET flow control, the following approaches can be explored. Since the like-charge repulsion keeps the molecules away from the walls, at least in the absence of the gate bias, one can maintain the pH of the buffer solution well above the isoelectric point of both channel walls and molecules, thus keeping them negatively charged. Conversely, the buffer pH can be maintained well below the isoelectric point of both channel walls and molecules to keep them both positively charged. Another viable solution is to tailor the surface functional groups of SiO<sub>2</sub> channel walls that minimize non-specific adsorption of charged molecules. Ideally, these functional groups must have an isoelectric point very close to but slightly below the desired buffer pH, which enables pronounced FET electroosmotic flow control.<sup>11</sup> These functional groups include a variety of polymers, such as polyethylene glycol (PEG) and polyethylene terephthalate (PET).<sup>39–41</sup> For instance, the isoelectric point of PEG is 6.2.<sup>40</sup>

## Conclusions

We have fabricated nanofluidic MIR infrared waveguides integrated with an array of nanochannels, whose top window is optically transparent. This device architecture provides a capability to simultaneously monitor the flow control and probe molecule–wall interactions, using LS-CFM and MIR-FTIRS. The surface charge, and therefore  $\zeta$ -potential, are modulated in a fluidic FET configuration. The flow control of charged dye molecules (Rhodamine B) in nanochannels is achieved by modulating the surface charge. With LS-CFM imaging, we observe that the flow of Rhodamine B either accelerates or decelerates in response to the negative and positive gate bias, respectively. We also observe that positively charged Rhodamine B, while the channel walls (SiO<sub>2</sub>) are negatively charged, shows strong electrostatic dye–wall interactions. Depending on the polarity and magnitude of the gate bias, this dye–wall interaction is controlled and monitored along with the direction of the electroosmotic flow, using MIR-FTIRS. In an extreme case, we observe that the dye–wall interaction of positively charged Rhodamine B leads to irreversible wall adsorption. The adsorbed Rhodamine B is only partially desorbed, even after a strongly positive gate bias of +30 V is applied. The implication of this charge-dependent molecule–wall interaction is that the polarity and magnitude of channel surface charge significantly influences the mobility of charged molecules in nanochannels and that this mobility control can be used as an additional mechanism to separate the molecules. In the future, we will further examine the impact of molecule–wall interactions, using fluorescent dye molecules of similar molecular weight that assume different charges as a function of pH.

## Acknowledgements

The authors thank the National Science Foundation Nanoscale Interdisciplinary Research Team Program (CTS-0404124) for their financial support and W. M. Keck Foundation for providing support to establish a laser-scanning confocal fluorescence microscopy laboratory. The authors also wish to thank Qiming Li for initially helping with the nanochannel fabrication. This work is also supported by the Korea Research Foundation Grant funded by the Korean Government (MOEHRD, KRF-2006-214-D00034).

## References

- 1 A. Daridon, M. Sequeira, G. Pennarun-Thomas, H. Dirac, J. P. Krog, P. Gravesen, J. Lichtenberg, D. Diamond, E. Verpoorte and N. F. de Rooij, *Sens. Actuators, B*, 2001, **76**, 235–243.
- 2 A. Manz, N. Graber and M. H. Widmer, *Sens. Actuators, B*, 1990, **1**, 244–248.
- 3 A. van den Berg and T. S. J. Lammerink, *Top. Curr. Chem.*, 1998, **194**, 21–49.
- 4 D. J. Harrison, K. Fluri, K. Seiler, Z. Fan, C. S. Effenhauser and A. Manz, *Science*, 1993, **261**, 895–897.
- 5 S. Liu, Y. Shi, W. W. Ja and R. A. Mathies, *Anal. Chem.*, 1999, **71**, 566–573.
- 6 R. A. Mathies, P. C. Simpson and A. T. Woolley, in *DNA Analysis with Capillary Array Electrophoresis Microplates, Micro Total Analysis Systems*, ed. D. J. Harrison and A. van den Berg, Kluwer Academic Publishers/Banff, Canada, 1998, pp. 1–7.
- 7 P. C. Simpson, D. Roach, A. T. Woolley, T. Thorsen, R. Johnston, G. F. Sensabaugh and R. A. Mathies, *Proc. Natl. Acad. Sci. U. S. A.*, 1998, **95**, 2256–2261.
- 8 N. L. Anderson, A. D. Matheson and S. Steiner, *Curr. Opin. Biotechnol.*, 2000, **11**, 408–412.
- 9 G. Grandi, *Trends Biotechnol.*, 2001, **19**, 181–188.
- 10 J. H. Wang and R. M. Hewick, *Drug Discovery Today*, 1999, **4**, 129–133.
- 11 R. B. M. Schasfoort, S. Schlautmann, L. Hendrikse and A. van den Berg, *Science*, 1999, **286**, 942–945.
- 12 J. C. T. Eijkel and A. van den Berg, *Microfluid. Nanofluid.*, 2005, **1**, 249–267.
- 13 R. Fan, R. Karnik, M. Yue, D. Li, A. Majumdar and P. Yang, *Nano Lett.*, 2005, **5**, 1633–1637.
- 14 R. Karnik, R. Fan, M. Yue, D. Li, P. Yang and A. Majumdar, *Nano Lett.*, 2005, **5**, 943–948.
- 15 K. Ghowsi and R. J. Gale, *J. Chromatogr.*, 1991, **559**, 95–101.
- 16 K. Ghowsi and R. J. Gale, *J. Am. Lab.*, 1991, **23**, 17–20.
- 17 L. J. Guo, X. Cheng and C.-F. Chou, *Nano Lett.*, 2004, **4**, 69–73.
- 18 R. Karnik, K. Castelino, R. Fan, P. Yang and A. Majumdar, *Nano Lett.*, 2005, **5**, 1638–1642.
- 19 V. G. Kutchoukov, L. Pakula, G. O. F. Parikesit, Y. Garini, L. K. Nanver and A. Bossche, *Sens. Actuators, A*, 2005, **123–124**, 602–607.
- 20 K. F. Lei, S. Ahsan, N. Budraa, W. J. Li and J. D. Mai, *Sens. Actuators, A*, 2004, **114**, 340–346.
- 21 J. L. Pearson and D. R. S. Cumming, *Microelectron. Eng.*, 2005, **78–79**, 343–348.
- 22 K. Kobayashi, H. Unno, H. Takizawa and S. Adachi, *Jpn. J. Appl. Phys.*, 1996, **35**, 5925–5928.
- 23 E. H. Anderson, G. M. Horwitz and H. I. Smith, *Appl. Phys. Lett.*, 1983, **43**, 874–875.
- 24 W. C. Cheng, L. A. Wang and C. Y. Hsieh, *Microelectron. Eng.*, 2003, **67–68**, 63–69.
- 25 L. F. Johnson, G. W. Kammlott and K. A. Ingersoll, *Appl. Opt.*, 1978, **17**, 1165–1181.
- 26 S. Zaidi and S. R. J. Brueck, *Proc. SPIE*, 1999, **3740**, 340–343.
- 27 S. H. Zaidi and S. R. J. Brueck, *J. Vac. Sci. Technol., B*, 1993, **11**, 658–666.
- 28 S. M. Han and E. S. Aydil, *J. Electrochem. Soc.*, 1997, **144**, 3963–3967.
- 29 Y.-J. Oh, S. M. Cho and C.-H. Chung, *J. Electrochem. Soc.*, 2005, **152**, C348–C355.
- 30 E. D. Palik, *Handbook of Optical Constants of Solids*, Academic Press, Orlando, 1985, pp. 571–586 and pp. 479–763.
- 31 M. Kosmulski and E. Matijevic, *Langmuir*, 1992, **8**, 1060–1064.
- 32 A. Garcia, L. K. Ista, D. Petsev, M. J. O'Brien, P. Bisong, A. A. Mammoli, S. R. J. Brueck and G. P. López, *Lab Chip*, 2005, **5**, 1271–1276.
- 33 K. F. Schrum, J. M. Lancaster, S. E. Johnston and S. D. Gilman, *Anal. Chem.*, 2000, **72**, 4317–4321.
- 34 Y. J. Maréchal, *Phys. Chem.*, 1993, **97**, 2846–2850.
- 35 N. Watanabe, T. Horii and A. Kouchi, *Astrophys. J.*, 2000, **541**, 772–778.
- 36 C. J. Pouchert, *The Aldrich library of FT-IR spectra*, Aldrich Chemical Co., 1985, vol. 2, p. 1014A.
- 37 M. Pospisil, P. Čápková, H. Weissmannová, Z. Klika, M. Trchová, M. M. Chmielová and Z. Weiss, *J. Mol. Model.*, 2003, **9**, 39–46.
- 38 Y. Marécahl, *J. Chem. Phys.*, 1991, **95**, 5565–5573.
- 39 J. S. Rossier, G. Gokulrangan, H. H. Girault, S. Svojanovsky and G. S. Wilson, *Langmuir*, 2000, **16**(22), 8489–8494.
- 40 H. Bi, S. Meng, Y. Li, K. Guo, Y. Chen, J. Kong, P. Yang, W. Zhong and B. Liu, *Lab Chip*, 2006, **6**, 769–775.
- 41 E. A. S. Doherty, R. J. Meagher, M. N. Albarghouthi and A. E. Barron, *Electrophoresis*, 2003, **24**(1–2), 34–54.